

# The Minimum Length Scale for Evaluating QG Omega Using High-Resolution Model Data

MICHAEL BATTALIO

*Department of Atmospheric Science, Texas A&M University, College Station, Texas*

JAMIE DYER

*Department of Geosciences, Mississippi State University, Mississippi State, Mississippi*

(Manuscript received 27 June 2016, in final form 25 October 2016)

## ABSTRACT

The minimum length scale to investigate quasigeostrophic (QG) vertical motion within a mesoscale operational model is determined using simulations of 28 baroclinic systems from the North American Mesoscale Forecast System (NAM) model. Two upscaling methods are tested to find the optimal QG characteristic length. The box method takes an average of each field before performing finite-differencing calculations. The cross method samples the data at increasing distances between finite-difference calculations. The traditional QG omega equation is evaluated with each upscaling technique and found to be reliable between 800 and 200 hPa. The minimum QG length scale is found to be  $L = 140$  km considering correlations of QG omega back to operational model values, which are  $0.48 \pm 0.05$  for both methods on an “extended” QG omega. The box method performs marginally better than the cross method due to a larger reduction of QG forcing in higher-order wavenumbers, but at the appropriate length scale, both methods have indistinguishable correlations.

## 1. Introduction

Meteorologists have relied upon the quasigeostrophic (QG) omega ( $\omega$ ) equation to diagnose and forecast vertical motion for decades (Billingsley 1997; Davies 2015). The current use of the QG  $\omega$  equation is confined to qualitative evaluation by operational forecasters and to the research community who quantitatively employs the  $\omega$  equation to ascertain sources of synoptic-scale forcing. The QG  $\omega$  equation estimates two drivers for vertical motion: thermal advection (TA) and differential vorticity advection (VA) (Trenberth 1978).

QG  $\omega$  is used frequently due to the straightforward interpretation of its forcing functions. However, when evaluating QG  $\omega$ , many studies fail to take into account the increased resolution of model and reanalysis datasets, instead applying QG  $\omega$  to data that are of higher-resolution than what can be evaluated assuming quasi-geostrophy. Some studies do account for the necessity of coarse data when applying the QG approximation, but many recent studies have used the QG  $\omega$  equation on unsmoothed,

fine-gridded reanalysis or model data. If the QG  $\omega$  equation is applied to data that are of too high resolution, the resulting vertical motions can be unphysical and nonsensical. It is vital to determine the appropriate horizontal scale at which QG theory can be successfully implemented using methods that extract data from the mesoscale models themselves rather than simply filtering the data.

Given the applicability of QG  $\omega$  and the inexorable move toward higher-resolution numerical weather model output, two questions are posed: What is the appropriate horizontal length scale to find QG  $\omega$  using high-resolution datasets? What methods can reliably extract synoptic-scale vertical motion from mesoscale data? The traditional QG  $\omega$  equation is applied to 28 recent synoptic-scale events, simulated by the operational North American Mesoscale Forecast System (NAM) model, using two upscaling techniques to find the minimum applicable horizontal scale based on correlations to NAM-simulated values of vertical motion.

## 2. Background

QG  $\omega$  has been shown to work well in diagnosing synoptic-scale vertical forcing. Pauley and Nieman

---

*Corresponding author e-mail:* Michael Battalio, michael@battalio.com

(1992) compared the QG  $\omega$  equation to a generalized  $\omega$  equation used by Krishnamurti (1968) and found that if terms of higher-order Rossby number were neglected, the generalized  $\omega$  reduced to the QG form. Räisänen (1995) continued the work by correlating the generalized  $\omega$  equation to QG  $\omega$  and found that correlations increased as latitude increased, and while diabatic processes dominated in the tropics, TA and VA were the primary forcing mechanisms in the midlatitudes. Vasilj and Smith (1997) used QG  $\omega$  to evaluate the Zwack–Okossi development equation (Zwack and Okosssi 1986) and demonstrated that it performed as well as a generalized, “extended” form in diagnosing surface pressure tendencies. Others have used the QG  $\omega$  equation in synoptic-scale case studies of extratropical cyclones and have found that the QG  $\omega$  equation provides useful information in diagnosing storm structure and development. Sinclair (1993) used QG  $\omega$  to study extratropical behavior of a tropical cyclone and established that the strongest ascent occurred where VA and TA acted in phase. Smith and Lin (1978) provided a comparison of three estimates of vertical motion: kinematic, general  $\omega$ , and traditional QG  $\omega$  using a skill score and correlation to accumulated rainfall. The kinematic solution performed better than the  $\omega$  solutions, and the QG  $\omega$  performed better than the general  $\omega$ . Since it was developed, the  $\omega$  equation has provided the backbone of many vertical-motion diagnostics (e.g., Gyakum 1991; Lupo et al. 1992).

More recent studies have used QG  $\omega$  as a tool to study other phenomena instead of the nature of vertical motion itself. While studies before roughly the year 2000 have calculated QG  $\omega$  on datasets of low resolution, recent studies using the native resolution of reanalysis datasets calculate  $\omega$  approaching the lowest theoretical limit of QG theory. The 2.5° (196 km at 45°N) NCAR–DOE reanalysis was used by Hart et al. (2010) to calculate QG  $\omega$  to study African summer rainfall, and Hryciw et al. (2013) calculated QG  $\omega$  on the 2.5° (196 km at 45°N) NCEP–NCAR reanalysis to investigate drought on the Canadian prairie. Lareau and Horel (2012) diagnosed storm tracks over western North America with QG  $\omega$  on a 1.5° (118 km at 45°N) dataset, acknowledging that 1.5° data were specifically used instead of higher-resolution data to minimize subsynoptic-scale features. Finch and Johnson (2010) calculated QG  $\omega$  on a 1° (79 km at 45°N) gridded dataset to investigate the North American monsoon, finding temperature advection to be the most important driver. A 1° (79 km at 45°N) dataset, the GFS FNL, was used by Gao et al. (2009) to find QG vertical forcing on landfalling tropical systems in China. The  $\mathbf{Q}$  vectors were calculated on the 32-km North American Regional Reanalysis by Milrad et al. (2010) and Ressler et al. (2012) to study Canadian

cool-season precipitation and freezing rain events, respectively.

While none of these studies directly addressed the horizontal spacing of grid points, some other selected studies have. Lang and Martin (2010) and Martin (2014) used 1° data (79 km at 45°N) but performed a Gaussian smoothing to eliminate 2/3 of the power in wavelengths less than 660 km. Surcel et al. (2016) specifically used a coarser NCEP reanalysis at 210-km resolution to calculate  $\mathbf{Q}$  vectors.

The filtering of synoptic-scale diagnostics from mesoscale models was first attempted by Barnes et al. (1996). Using the  $\mathbf{Q}$ -vector form of the QG  $\omega$  equation (Hoskins et al. 1978), forcing from mesoscale gravity waves was found to be up to two orders of magnitude larger than synoptic-scale forcing. Gravity waves were removed from 29-km Eta Model (now NAM) pressure and geopotential height fields by implementing a cowbell spectral filter for each grid point with an  $N \times N$  footprint. With the gravity wave influence removed, synoptic-scale forcing was resolved at a  $15 \times 15$  grid scale. This analysis was limited to only the QG  $\omega$  forcing function, not the vertical motion itself. Even though the QG  $\omega$  field is a linear function of the total three-dimensional forcing, the local values of  $\omega$  are not linearly proportional to the local forcing (Durrán and Snellman 1987); thus, the QG forcing functions, as well as the vertical motion field itself, are investigated here.

Any numerical assessment of QG theory must remain within the length scales where geostrophy is valid, usually evaluated with the Rossby number. The Rossby number is the ratio of the acceleration (inertial) and Coriolis force terms, and values of the Rossby number must be much smaller than 1 for geostrophy to be valid. QG theory places two constraints on the relative magnitudes of variables using the Rossby number (Holton 2004). First,  $Ro = U/(f_0 L)$ —where  $U$  is the characteristic horizontal wind speed,  $L$  is the characteristic length scale, and  $f_0$  is the Coriolis parameter—implies that inertial accelerations are small relative to Coriolis accelerations. Second,  $Ro = \beta \times L/f_0$  implies that the variation of the Coriolis acceleration with latitude,  $\beta \times L$ , is smaller than the Coriolis parameter  $f_0$ . Setting those two terms equal to one another generates an expression for the horizontal length scale:  $L \approx \sqrt{U/\beta}$ . To obtain appropriate values of  $Ro$  assuming typical values of baroclinic waves,  $U \approx 10 \text{ m s}^{-1}$  and  $\beta \approx 1 \times 10^{-11} \text{ m}^{-1} \text{ s}^{-1}$ , the length scale must be greater than or equal to 1000 km. Using the approximation that five grid points are needed to resolve a feature well, the smallest useful spacing is  $L \approx 200 \text{ km}$ , far larger than most operational models and many reanalysis datasets and larger than or of the same size as many of the studies previously mentioned. Such a scale length suggests that raw reanalysis or model fields should not be used to perform

QG analysis. We aim to provide an empirical estimate of the smallest usable resolution in calculating QG  $\omega$ .

### 3. Evaluation of $\omega$

Rapid and widespread evaluation of  $\omega$  is hindered by two problems. First, the appropriate length scale over which to evaluate the QG  $\omega$  forcing functions must be determined. Second, if the goal is to compare a QG form of  $\omega$  to a model-derived  $\omega$ , the question must be answered of how best to upscale the high-resolution fields to lower resolutions where quasi geostrophy is valid.

#### a. The QG $\omega$ equation

The QG  $\omega$  equation was developed in response to a need for vertical motion estimations from only horizontal wind and height observations (Sutcliffe 1947; Wiin-Nielsen 1959; Trenberth 1978). Many forms of the  $\omega$  equation have been developed, including the traditional QG form (Fjørtoft 1955), the Sutcliffe–Trenberth approximation (Sutcliffe 1947; Trenberth 1978), the  $\mathbf{Q}$ -vector form (Hoskins et al. 1978), and various general  $\omega$  equations (e.g., Krishnamurti 1968). The QG  $\omega$  formulation has been found to be quite similar to primitive equation assessments of vertical motion that are controlled to a large extent by physical processes included within QG theory (Mudrick 1974; Barnes and Colman 1993; Jusem and Atlas 1998). Räisänen (1995), Zwack and Okoski (1986), and Vasilj and Smith (1997) found that the dominant forcing terms in the general  $\omega$  equation when  $Ro > 0.1$  were those of vorticity advection and thermal advection, which are the two QG  $\omega$  forcing terms.

The traditional QG  $\omega$  equation is derived from mass continuity, the QG vorticity equation, the thermodynamic energy equation, and the ideal gas law (Holton 2004). Under certain assumptions, including but not limited to horizontally uniform static stability,  $Ro \ll 1$ , and hydrostatic balance, the traditional QG  $\omega$  equation is

$$\underbrace{\left(\frac{\sigma}{f_0^2} \nabla_h^2 + \frac{\partial^2}{\partial p^2}\right)}_A \omega = \underbrace{\frac{1}{f_0} \frac{\partial}{\partial p} [\mathbf{V}_g \cdot \nabla_h (\zeta_g + f)]}_B + \underbrace{\frac{1}{f_0^2} \nabla_h^2 \left[ \mathbf{V}_g \cdot \nabla_h \left( \frac{RT}{p} \right) \right]}_C, \quad (1)$$

where  $\omega$  is the vertical velocity,  $\sigma = -(RT/P)[d(\ln\theta_0)/dP]$  is the static stability parameter,  $\zeta_g$  is the geostrophic relative vorticity,  $p$  is the pressure,  $f_0$  is the Coriolis parameter,  $\mathbf{V}_g$  is the geostrophic wind, and the subscript  $h$  denotes horizontal operators.

On the right-hand side (rhs), terms B and C are the forcing functions of  $\omega$  and represent differential vorticity

advection with height and thermal advection, respectively. Upward motion occurs where cyclonic vorticity advection increases with height or in areas of warm air advection. The left-hand side (lhs) of the  $\omega$  equation is a form of the three-dimensional Laplacian in pressure coordinates. For qualitative assessments, it is assumed that the vertical motion can be described by summations of sine waves in every direction so that the lhs operator is proportional to  $-1$  for each individual wavenumber, and term A is reduced to  $-\omega$  (Wiin-Nielsen 1959). However, outside of a layer between 400 and 600 hPa, this qualitative assessment of  $\omega$  is not valid (Durran and Snellman 1987). Not included in the present study is an investigation of the diabatic forcing of the omega equation. Räisänen (1995) showed that the diabatic term is 20%–40% smaller than the other forcing functions in the midlatitudes in winter, but Pauley and Nieman (1992) showed that in strong marine cyclones diabatic effects may be stronger than vorticity or thermal advection. However, few studies use the diabatic term in synoptic diagnosis, and since we are primarily investigating continental cyclones, the diabatic term is not considered here. Furthermore, diabatic forcing has been found to be in phase with the forcing from the vorticity and thermal advection terms, only reinforcing the adiabatic forcing (Davies 2015).

In calculating the rhs, the geostrophic wind was used to find the vorticity and the advection. However, many datasets have the full horizontal wind available, so  $\omega$  was calculated a second time using the full wind (i.e., substituting  $\mathbf{V}$  for  $\mathbf{V}_g$ ). Replacing the geostrophic wind with the full wind has been used by Tsou and Smith (1990) and Vasilj and Smith (1997) and expands the usability of the interpretation to ageostrophic motions. It will be referred to as the extended form of the QG  $\omega$  equation. Tsou et al. (1987) provide a scale analysis of terms for the QG height tendency equation to arrive at a version of the QG  $\omega$  equation using both geostrophic and ageostrophic winds. Static stability was calculated as an average value at each pressure level, and the Coriolis parameter was allowed to vary with latitude. Both the geostrophic and extended versions are compared in the results.

The traditional form of the QG  $\omega$  equation is mathematically identical to the  $\mathbf{Q}$ -vector approach of Hoskins et al. (1978); therefore, as the objective of this paper is to quantify vertical motion as opposed to only a subjective analysis of the forcing features, the  $\mathbf{Q}$ -vector approach is redundant to the traditional formulation and is not evaluated.

#### b. Numerical methods for calculating $\omega$

The traditional form of the QG  $\omega$  equation [Eq. (1)] using both the geostrophic forcing and extended versions was evaluated for each case. Interior horizontal derivatives were calculated with sixth-order, centered finite-differencing. Along the boundaries, fourth-order,

forward/backward finite differencing was used. The outer 30 grid cells were discarded to eliminate reflections. In the vertical, second-order, centered finite differencing was used inside the domain, and second-order, forward/backward finite differences were used at the top and bottom levels with values set to zero below the surface. For each QG  $\omega$  calculation, the potential temperature, static stability, vorticity, divergence, and geostrophic winds were first calculated.

On the lhs, the method of sequential relaxation inverted the three-dimensional Laplacian operator. Two sets of initial conditions were applied to the relaxation solution. As a first guess, homogeneous initial conditions across the entire domain were applied. The method of sequential relaxation requires large computational resources, so a kinematic initial condition was used for the interior of the domain for the extended version of the  $\omega$  equation to hasten convergence. Numerical solutions to the kinematic initial condition involved integrating the pressure-weighted, horizontal divergence throughout the atmospheric column and included a second-order adjustment to the vertical motion by scaling the wind field such that the condition  $\omega = 0$  was imposed at 50 hPa (O'Brien 1970). The lower boundary condition was fixed at zero for the kinematic initial condition. The geostrophic-forced version used homogeneous initial conditions. Both the homogeneous condition and heterogeneous condition yielded near identical results for the primary case study, so all subsequent calculations used only the heterogeneous initial condition for extended QG  $\omega$ .

As suggested by Stuart and Neill (1967), a relaxation factor of  $\alpha = 0.3$  most quickly induced convergence to a solution. The convergence was determined by comparing the correlations of QG  $\omega$  to NAM  $\omega$  for both the kinematic and homogeneous initial conditions. Iterations ended when the difference between successive relaxation solutions of the extended  $\omega$  was less than  $\pm 1 \text{ nPa s}^{-1}$  for the entire domain. Such a stringent condition required approximately 10 000 iteration loops. Convergence to the solution was checked by comparing the correlation between NAM  $\omega$  and the extended QG  $\omega$  with the kinematic initial condition to the correlation between NAM  $\omega$  and the extended QG  $\omega$  with the homogeneous initial condition for one case study first. The difference between the two values on average was less than 0.01. Similar convergence conditions were achieved with the geostrophic  $\omega$  when the difference between successive relaxation solutions was less than  $\pm 100 \text{ pPa s}^{-1}$ .

#### 4. Data and computations

The operational NAM model was used for testing of  $\omega$  due to the high horizontal resolution, large extent, and widespread operational acceptance of the model. A 6-h

forecast was used to ensure consistency of the model dynamics and to avoid initialization shock. The NAM provides an approximately  $12 \text{ km} \times 12 \text{ km} \times 25 \text{ hPa}$  grid across North America. Model data as opposed to re-analyses were used due to their higher resolution so that mesoscale lengths could be tested.

Two approaches were tested to evaluate the optimum horizontal scale of the  $\omega$  equations. Method one, hereafter referred to as the cross method, consisted of increasing the distance between points used in the finite-difference calculations from the nearest adjacent neighbor,  $s = 1$ , to successively more distant points. The cross method sampled the data at larger and larger distances, ignoring points in-between. Spacing from  $s = 1$  (defined as the native model resolution) up to  $s = 30$  was tested, corresponding to points 12 to 360 km away from the center point. The technique was applied to each rhs finite-difference calculation, to the sequential relaxation of the lhs Laplacian, and to the divergence of winds used in the kinematic initial condition.

The second method, referred to as the box method, is similar to the Barnes et al. (1996) grid-scaling technique. An  $N \times N$  average was evaluated around each grid cell, and the average was assigned as the value of the central grid cell. Grid sizes were tested from  $N = 1$  to  $N = 61$ , where the  $N = 1$  field was defined as identical to the  $s = 1$  field. For the rhs, the average was taken across each initial field and prior to each subsequent horizontal finite-difference calculation, as well as to the wind used in the kinematic  $\omega$ . Though the calculation of the box method is similar to that of Barnes et al. (1996), we apply the filter not only to the initial fields but to each subsequent horizontal difference calculation, as it is the scaling of the operators that should change not just the width of the smoothing function of the initial state variables. More importantly, we compare the final, inverted  $\omega$  instead of only the rhs forcing functions.

#### 5. Results

In total, five of the 28 cases were individually investigated to ascertain the length scale, which was then applied to the final 23 cases. The 1800 UTC 12 December 2010 case was carefully analyzed with a more cursory investigation of 1200 UTC 30 January 2013, 1200 UTC 30 March 2014, 1200 UTC 9 April 2014, and 1200 UTC 2 February 2015.

##### a. Case 1

The date 12 December 2010 was characterized by a prototypical midlatitude system with strong synoptic forcing across much of the eastern United States. A surface low with a central pressure of 988 hPa (not shown), with accompanying upper-level trough, strengthened over Lake Ontario at 1800 UTC. The trough was associated

with a pronounced jet stream at 300 hPa, with maximum winds of  $70 \text{ m s}^{-1}$  from the Georgia coast northward (Fig. 1a). An elongated vorticity maximum extended from Mississippi, through the base of the trough across Florida, Virginia, and into Ontario with multiple, local maxima and minima along the Atlantic coast (Fig. 1b). The accompanying warm air advection at 850 hPa was weak except for a small area over New England (Fig. 1c).

### 1) DIFFERENTIAL VORTICITY ADVECTION

The differential vorticity advection [Eq. (1) term B] at 500 hPa is shown in the extended form with the cross method (Figs. 2a–c) and box method (Figs. 2d–f) and using geostrophic winds with the cross method (Figs. 2g–i) and box method (Figs. 2j–l). The differences in horizontal extent of the minima and maxima of forcing at each spacing are evident. For example, at  $s = 3$  (Figs. 2a,g), there is a strong couplet of forcing near Washington, D.C. At  $s = 10$  (Figs. 2b,h), there is a minimum of forcing over Washington, D.C., while at  $s = 20$  (Figs. 2c,i) the minimum is broadened to encompass most of southern Pennsylvania. Generally, each forcing at  $s = 20$  is either spatially reduced or broken into further couplets of forcing at  $s = 10$  and is then reduced even further to more intense, closely spaced couplets at  $s = 3$ . Figures 2d–f show differential vorticity advection calculated using the box method and are similar to VA calculated by the cross method in horizontal scale (although more smoothed). The correlation between the two techniques decreases with increasing  $s$  and  $N$  (Table 1). The geostrophic versions of both the cross and box methods display forcing of similar horizontal extent but reduced magnitude as indicated by the mean absolute value (see panel headings of Fig. 2), with stronger forcing at the base of the trough as opposed to the exit region, which could be due to gradient balance caused by the high curvature in the base of the trough. The similarity between the extended and geostrophic forcing at small spacings compared to large  $s$  or  $N$  could be due to numerical noise arising from the calculation of geostrophic variables that artificially amplifies the geostrophic forcing at smaller horizontal scales.

In contrasting the three grid spacings, the decrease in magnitude of forcing as the grid spacing increases is of relevance. There is approximately one order of magnitude difference in the size of VA forcing between  $s = 3$  and 20. This behavior can be explained through a nonlinear scaling of the winds with distance:

$$\Delta v \approx \varepsilon^{1/3} \Delta x^{1/3}, \quad (2)$$

where  $\Delta x$  is the horizontal distance,  $\Delta v$  is the wind difference, and  $\varepsilon$  is the turbulent energy flux (Kolmogorov

1941). We can use this relationship to see how the rhs terms of the traditional  $\omega$  equation would scale under increasing  $s$ . The horizontal difference operations performed on the horizontal wind in term B of the traditional  $\omega$  equation are the cross product, followed by the gradient. The vorticity is a wind difference divided by a horizontal distance ( $\Delta v / \Delta x$ ), and the gradient is that result divided by distance again ( $\Delta v / \Delta x^2$ ). (The vertical pressure derivative is not altered by the value of  $s$ .) From Eq. (2), the vorticity scales as  $(\Delta v / \Delta x) \sim \Delta x^{-2/3}$ , and its gradient scales as  $[\Delta v / \Delta(x^2)] \sim \Delta x^{-5/3}$ . Assuming  $\varepsilon = 0.001 \text{ m}^2 \text{ s}^{-3}$  (Lovejoy and Schertzer 2010), Eq. (2) gives an average vorticity gradient on the order of  $10^{-10} \text{ m}^{-1} \text{ s}^{-1}$  for  $s = 20$ , which is close to the geostrophic mean absolute value (Figs. 2i,l). At  $s = 3$ , an estimate of  $3 \times 10^{-9} \text{ m}^{-1} \text{ s}^{-1}$  is obtained, which is close in magnitude to the  $9 \times 10^{-9} \text{ Pa}^{-1} \text{ s}^{-1}$  found for both the geostrophic and extended vorticity advection, capturing the decrease in order of magnitude as distance increases. From the headings in Figs. 2g and 2i, the magnitude of the geostrophic forcing ratio is 24, which exactly coincides with theory, as  $(20/3)^{5/3} \approx 24$ , while the ratio for the extended omega is somewhat smaller at  $\sim 7$ .

### 2) THERMAL ADVECTION

Thermal advection calculated by term C of the  $\omega$  equation has minima and maxima in a similar spatial pattern to VA. Figures 3a–c show the extended TA at 500 hPa using the cross method. The large-scale pattern consists of areas of forcing in areas of the strongest flow. As with VA, the TA forcing field is granulated at  $s = 3$ , with forcing packets on the order of tens of kilometers and increasing to hundreds of kilometers at  $s = 10$  and 20. The couplet structure shown in the VA and TA is present in previous studies (Barnes and Colman 1993; Mudrick 1974) and is indicative of the crests and troughs of the waves behind the forcing at each respective length scale. The box method in the extended form (Figs. 3d–f) produces few differences from the cross method, but the correlation between the two techniques is smaller for TA than VA (Table 1). Again, the fields using the box method are smoother but of the same horizontal spacing as the cross method. There is much closer agreement between the extended and geostrophic versions (Figs. 3g–i) of the thermal advection than the differential vorticity advection because for term C only the advection is changed, whereas with term B both the advection and the vorticity itself are modified by substituting model winds for geostrophic winds.

### 3) TOTAL TRADITIONAL QG FORCING

The total extended QG  $\omega$  forcing function at 500 hPa using the cross method is shown in Figs. 4a–c. At smaller

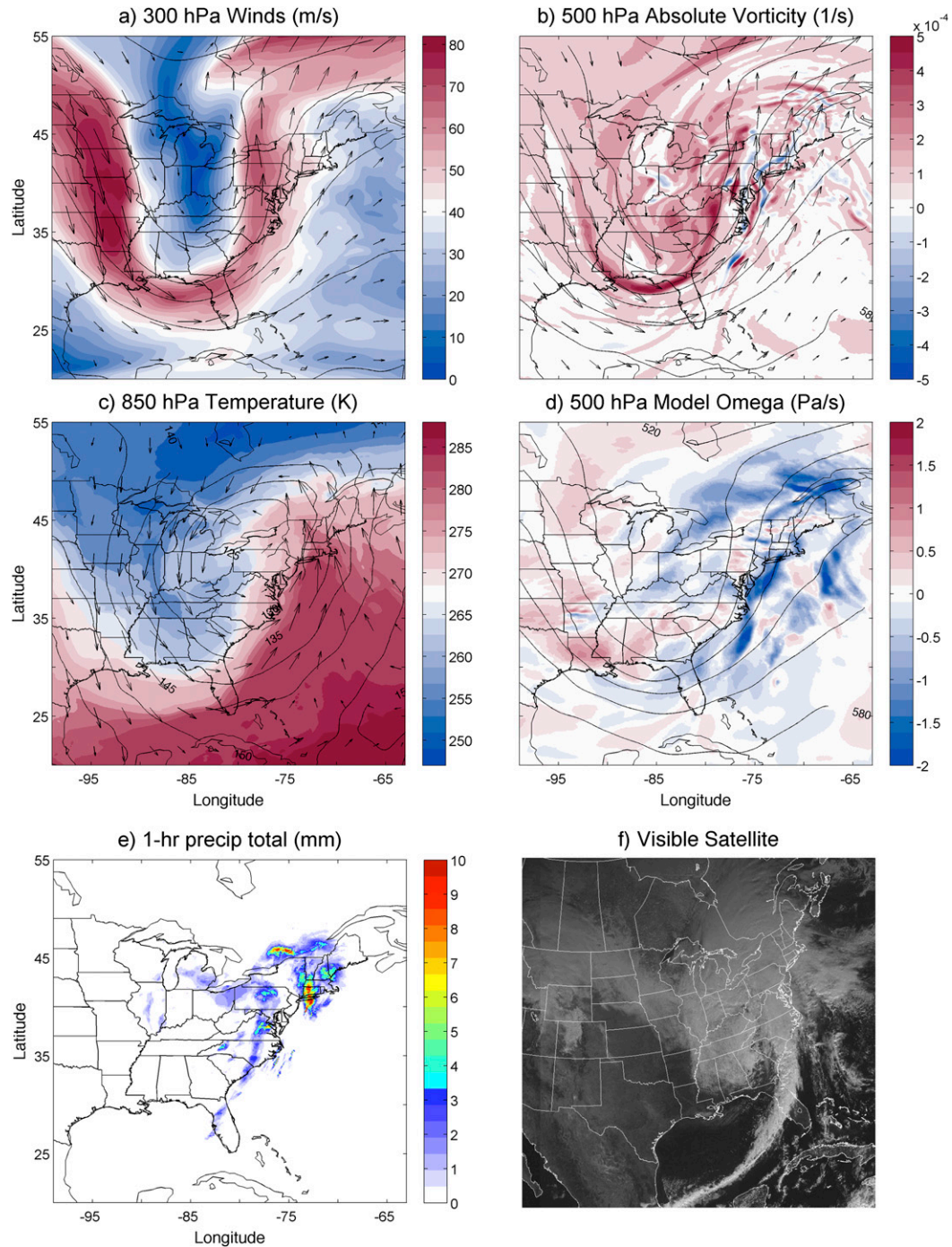


FIG. 1. NAM analysis for 1800 UTC 12 Dec 2010. (a) Wind speed ( $m s^{-1}$ ), wind vectors, and 300-hPa heights (contours every 20 dam). (b) Absolute vorticity ( $s^{-1}$ ), wind vectors, and 500-hPa heights (contours every 10 dam). (c) Temperature (K), wind vectors, and 850-hPa heights (contours every 5 dam). (d) NAM vertical motion ( $Pa s^{-1}$ ) and 500-hPa heights (contours every 10 dam). (e) 1-h, radar-estimated precipitation total for 1800–1900 UTC. (f) Visible satellite image for 1800 UTC.

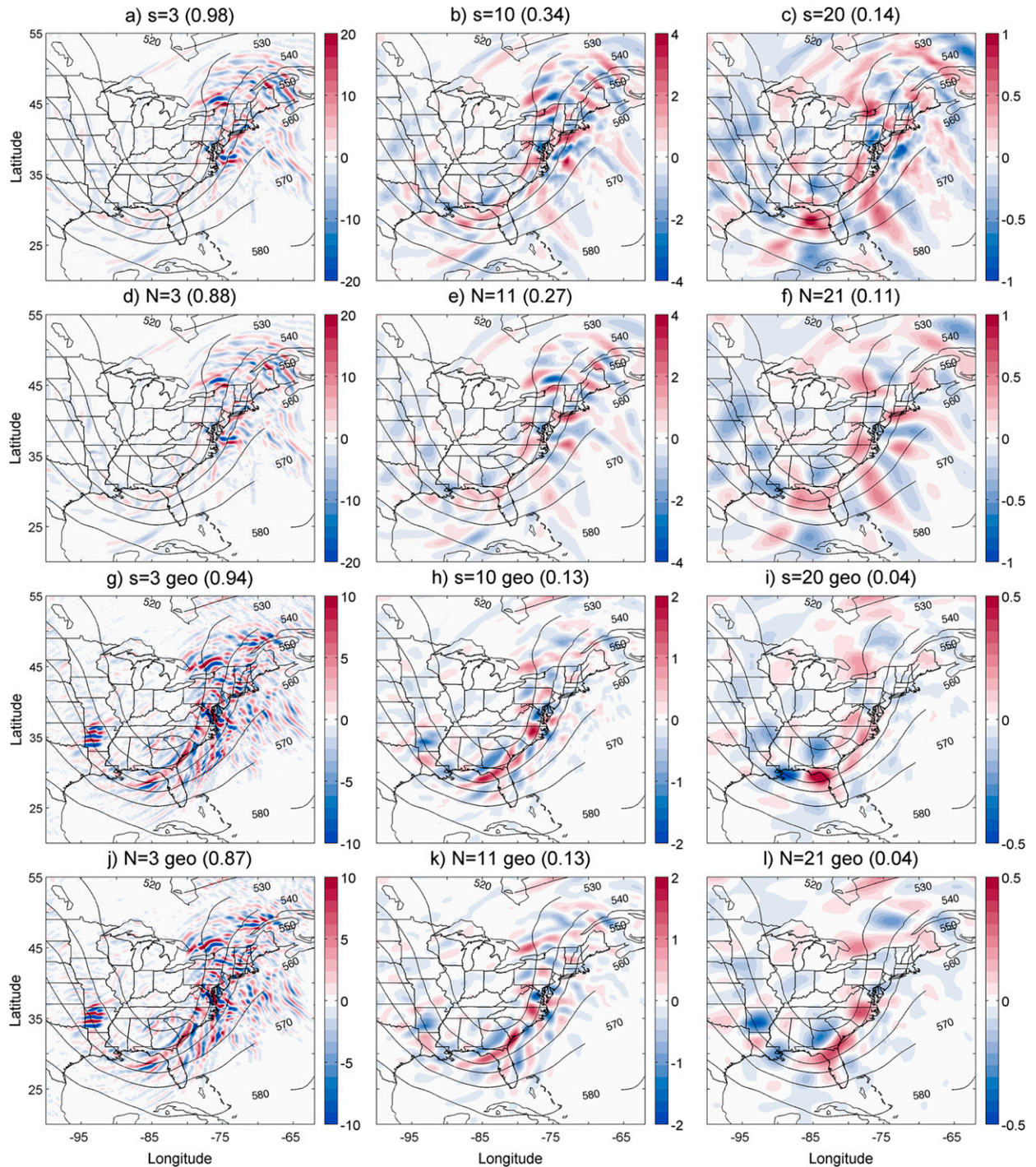


FIG. 2. Vorticity advection forcing ( $10^{-8} \text{ Pa}^{-1} \text{ s}^{-1}$ ), Eq. (1) term B at 500 hPa for 1800 UTC 12 Dec 2010. (Note the color scale is halved for the geostrophic panels, and the color scale decreases from the left column to the right as horizontal scale increases.) Cross method shown at (a),(g)  $s = 3$  (36-km separation); (b),(h)  $s = 10$  (120-km separation); and (c),(i)  $s = 20$  (240-km separation). Box method shown at (d),(j)  $N = 3$  (24-km box); (e),(k)  $N = 11$  (120-km box); and (f),(l)  $N = 21$  (240-km box). (a)–(f) use extended forcing; (g)–(l) use geostrophic forcing. Height contours are every 10 dam. Values in parentheses are average absolute value of field.

TABLE 1. Correlations between  $s$  and  $N$  values for each term of Eq. (1) and  $\omega$  on 1800 UTC 12 Dec 2010 at 500 hPa.

	$s = 3$	$s = 10$	$s = 20$
	$N = 3$	$N = 11$	$N = 21$
VA	0.98	0.87	0.71
TA	0.81	0.73	0.62
rhs	0.83	0.76	0.65
$\omega$	0.99	0.97	0.95

spacings (Fig. 4a), the individual packets of forcing are difficult to attribute to one mesoscale or synoptic-scale feature. At  $s = 10$  and 20, there is strong forcing through the entirety of the trough (Figs. 4b and 4c). At a spacing of  $s = 3$ , a prominent series of features (Figs. 4a,d,g,j) across central Arkansas is possibly the result of subsynoptic-scale forcing (e.g., gravity waves) as it is not captured by larger spacings. The extended QG forcing using the box method (Figs. 4d–f) shows much of the same forcing features as the cross method. There is reasonable agreement between the two methods of calculating the forcing function (Table 1). The geostrophic counterparts for the cross (Figs. 4g–i) and box (Figs. 4j–l) methods display forcing with the greatest magnitude near the base of the trough at the two larger grid spacings for each method; however, there is qualitative agreement between the extended and geostrophic versions for each method and spacing.

An averaged power spectrum of rhs forcing in the zonal direction shows that the power of higher wavenumber disturbances is removed for each of the two rescaling methods at larger spacings, while the power of lower wavenumbers is preserved (Figs. 5a and 5b). At larger spacings, both cross and box methods have comparable reduction in higher wavenumber power, but  $s = 3$  (Fig. 5a) shows almost no reduction in higher wavenumber power compared to  $N = 3$  (Fig. 5b). Also, the  $s = N = 3$  cases have less power at the lowest wavenumbers compared to intermediate wavenumbers, and the  $s = 3$  case shows little decrease in power even up to wavenumber 40. The geostrophic versions of forcing have less power across all wavenumbers compared to the extended forcing but the same pattern of reduced power at higher wavenumbers.

#### 4) TRADITIONAL QG $\omega$

Each QG vertical-motion field is compared to the operational NAM  $\omega$  (Fig. 1d). Figure 6 shows the correlation between QG  $\omega$  and NAM  $\omega$  at each level for  $s = 3, 10$  and  $N = 3, 11$ . The vertical distribution of correlation coefficients is similar between equal  $s$  and  $N$  values, and as  $s$  and  $N$  increase, correlations increase. At  $s = N = 3$  (Figs. 6a and 6c), correlations between QG  $\omega$  and NAM  $\omega$  are just below 0.6 for the extended QG  $\omega$  and just above

0.4 for the geostrophic QG  $\omega$  between 850 and 200 hPa. Above 200 hPa and below 850 hPa, correlations quickly drop to  $\sim 0.0$  for the geostrophic  $\omega$  and to  $\sim 0.3$  for the extended  $\omega$ . For  $s = 10$  and  $N = 11$ , correlations are highest for QG to model  $\omega$  between 200 and 800 hPa and range from 0.45 to 0.66 for the cross method (Fig. 6b) and the box method (Fig. 6d), with the cross method being slightly better around 500 hPa. The cross method with geostrophic winds has correlations to NAM  $\omega$  that are uniformly about 0.05 less than the extended QG  $\omega$ . In all four cases presented in Fig. 6, the extended QG  $\omega$  is uniformly higher than the geostrophic QG  $\omega$  correlation, and the  $s = N = 11$  correlations are higher than the  $s = N = 3$  correlations.

The total correlation for QG  $\omega$  and NAM  $\omega$  for all  $s$  and  $N$  values is shown in Fig. 7a for the cross method and Fig. 7b for the box method. Correlations increase with increasing  $s$  up to 20, then level off. The situation is similar for the box method, where correlations increase up to  $N = 21$ , then slowly decrease. The extended  $\omega$  reaches its maximum correlation much faster than the geostrophic  $\omega$ , but at large horizontal spacing they approach the same value. The geostrophic QG  $\omega$  correlations are about 0.2 less than the extended QG  $\omega$  correlations at the smallest horizontal scales, but the difference is only 0.05 at the largest horizontal scales.

QG  $\omega$  for 1800 UTC 12 December 2010 is shown in Fig. 8. The  $s = N = 3$  fields (Figs. 8a,d) show a general pattern of synoptic scale ascent in the cyclone with descent behind, but there are areas of strong descent embedded in the ascent. The strongest area is north of New York State and is associated with a strong couplet of forcing in southern Ontario (Figs. 4a and 4d). A second is off the coast of Washington, D.C., caused by a forcing couplet just off the eastern seaboard. Despite the areas of descent, the correlations back to NAM  $\omega$  are quite high (see headings of Fig. 8). Additionally, although the correlation between the  $s = 3$  and  $N = 3$  rhs forcing features is only 0.83, the correlation between the  $\omega$  values approaches 1 (Table 1). The geostrophic QG  $\omega$  (Figs. 8g,j) is much weaker than the extended QG  $\omega$  but has the same large-scale pattern. The areas of descent in the middle of the cyclone are absent, but there appear to be small-scale linear features of vertical motion over the Atlantic Ocean.

The general structure of QG  $\omega$  at longer horizontal length scales is more reasonable and consists of several areas of upward vertical motion. The  $s = 10$  and  $N = 11$  extended cases (Figs. 8b and 8e, respectively) show vertical motion associated with the main cloud shield (Fig. 1f) of the surface low and multiple local minima ahead of the cold front (Figs. 8b,e). There is also good agreement with the placement of the strongest precipitation totals (Fig. 1e) in New England and a local

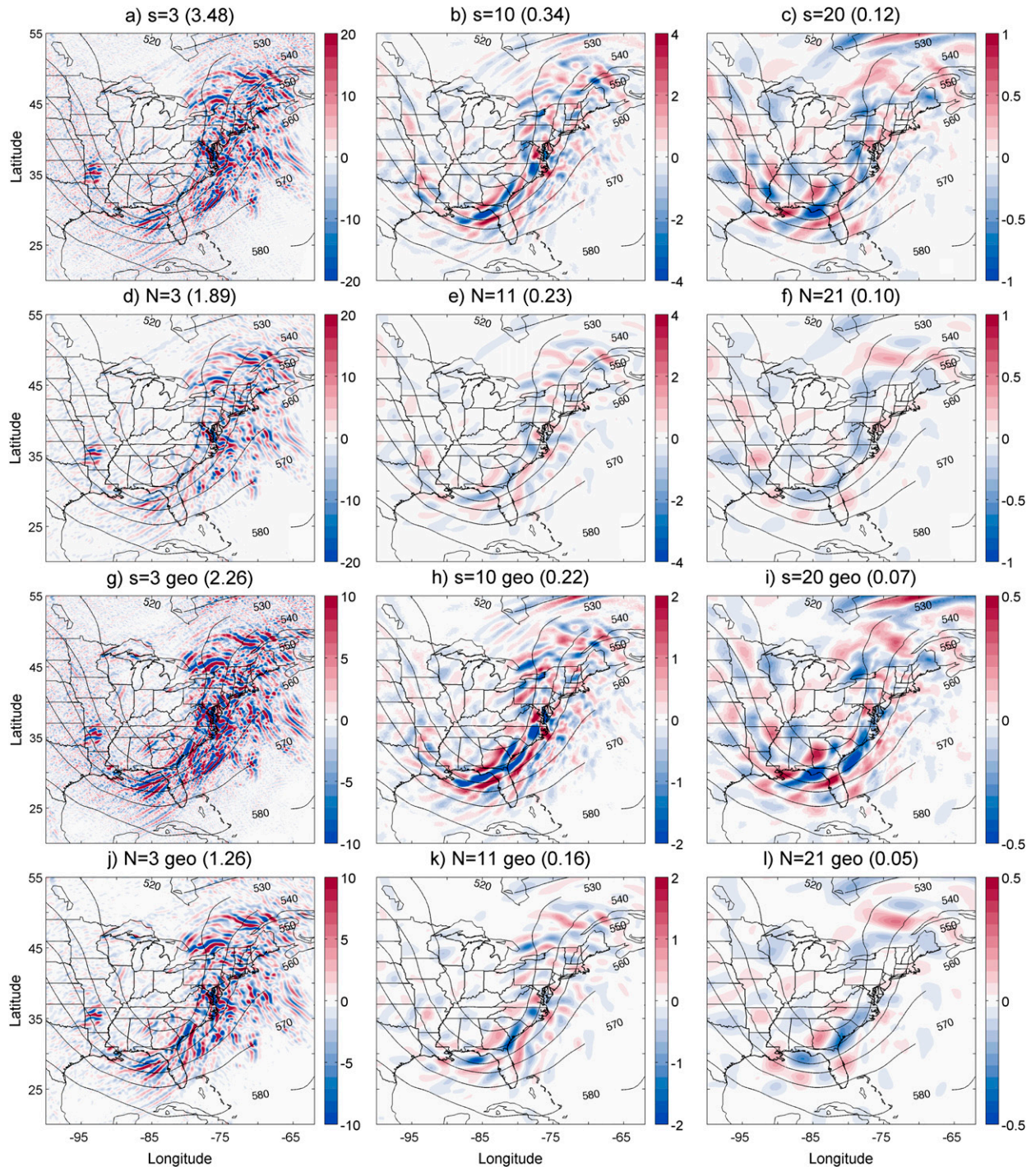


FIG. 3. As in Fig. 2, but with thermal advection forcing ( $10^{-8} \text{ Pa}^{-1} \text{ s}^{-1}$ ), Eq. (1) term C. (Note the color scale is halved for the geostrophic panels, and the color scale decreases from the left column to the right as horizontal scale increases.)

maximum of ascent. The correlation to the NAM  $\omega$  for the 500-hPa level at  $s = 10$  is 0.66 and 0.65 for  $N = 11$  (Figs. 6b and 6d, respectively), and the total column correlation remains nearly constant for values of  $s$  and  $N$  larger than 20 (Fig. 7). The  $s = 20$  and  $N = 21$  trials

(Figs. 8c and 8f, respectively) are more smoothed than the  $s = 10$  and  $N = 11$  cases, though the  $N = 21$  case more resembles the  $N = 11$  case than  $s = 20$  resembles  $s = 10$ . The larger length scale spreads the vertical motion across the entire eastern seaboard, but the

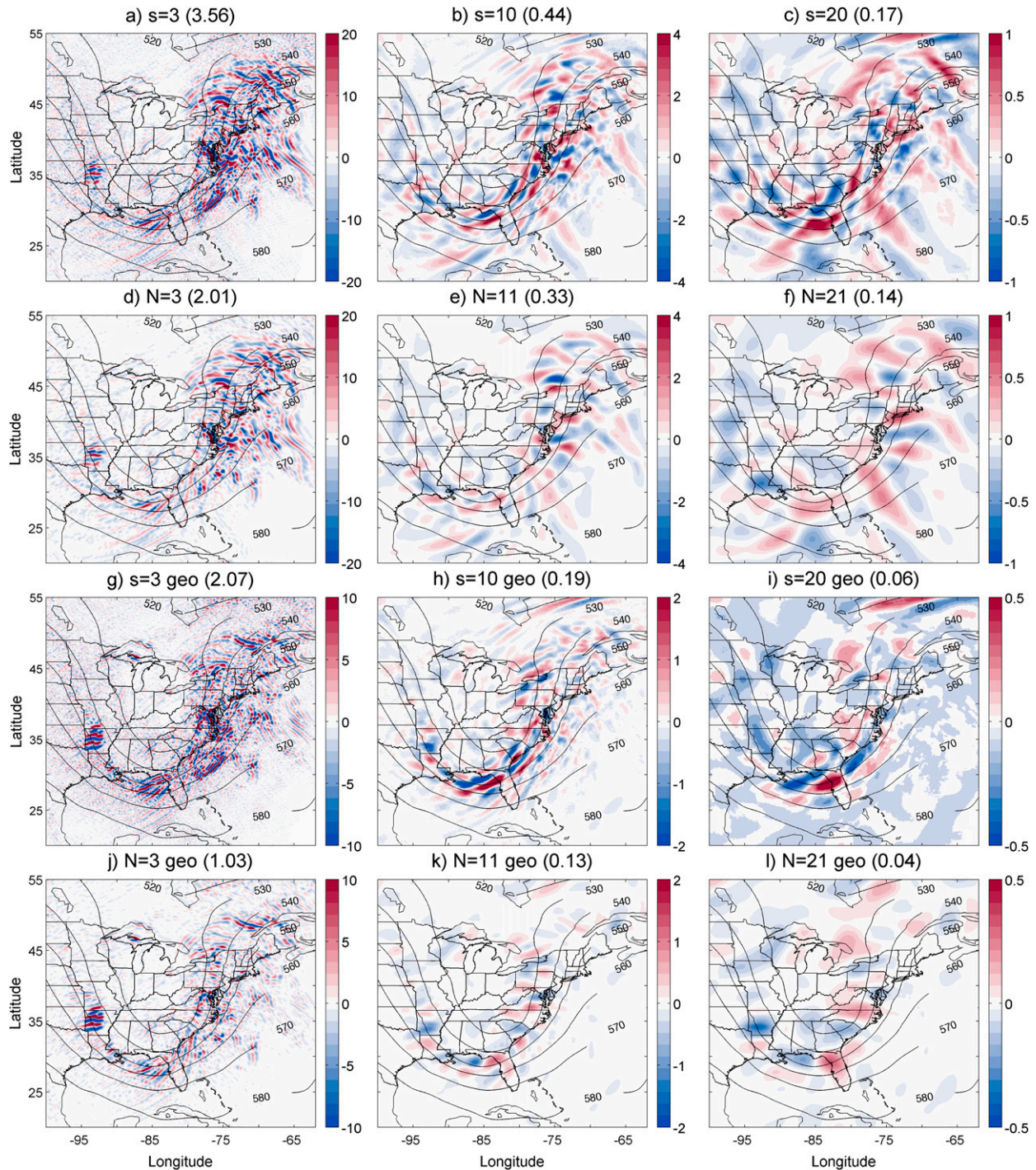


FIG. 4. As in Fig. 2, but with total QG forcing ( $10^{-8} \text{ Pa}^{-1} \text{ s}^{-1}$ ), Eq. (1) terms B and C. (Note the color scale is halved for the geostrophic panels, and the color scale decreases from the left column to the right as horizontal scale increases.)

individual local minima are still noticeable, especially with the box method. In general, the box method has higher magnitude maxima and minima than the corresponding cross method values. Even at the longer length scale, the correlations to NAM  $\omega$  are slightly higher. The

geostrophically forced counterparts (Figs. 8g–l) are in qualitative agreement with the extended versions but have weaker upward motion.

The power spectrum for  $\omega$  is shown in Figs. 5c and 5d. Unsurprisingly, as  $s$  or  $N$  increases, the power contained

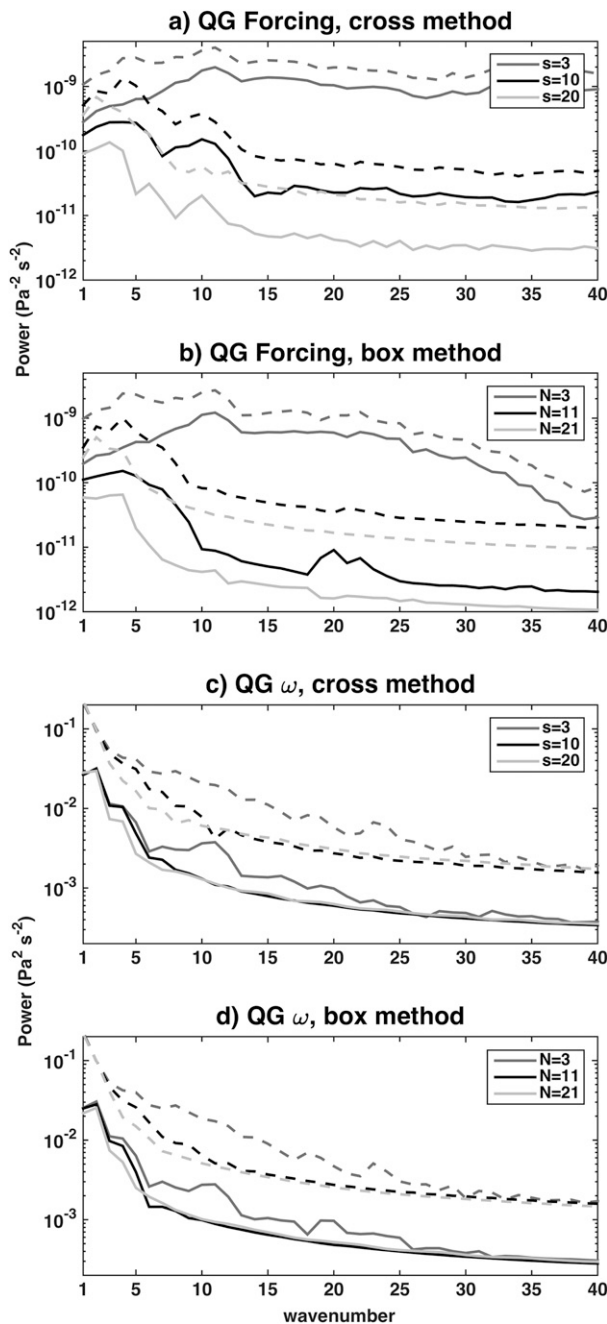


FIG. 5. Power spectra of QG forcing for 1800 UTC 12 Dec 2010 for the (a) cross method and (b) box method and of  $\omega$  for the (c) cross method and (d) box method. Solid lines correspond to geostrophic forcing; dashed lines correspond to extended forcing.

within higher wavenumbers is reduced. The box and cross methods show similar power spectra for almost all wavenumbers. Geostrophic QG  $\omega$  shows a greater reduction in the power across all wavenumbers compared to the extended QG  $\omega$ . The differences in power spectra for the geostrophic forcing functions and QG  $\omega$  are the

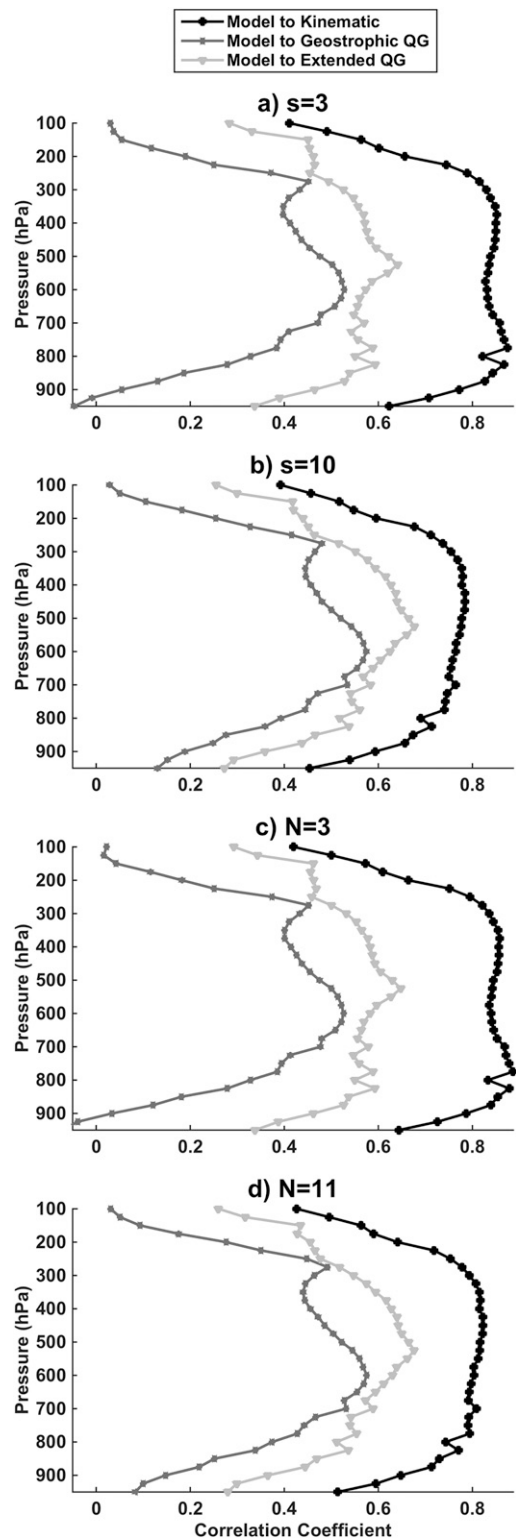


FIG. 6. Vertical correlations for 1800 UTC 12 Dec 2010 using the cross method for (a)  $s = 3$  and (b)  $s = 10$  and using the box method for (c)  $N = 3$  and (d)  $N = 11$ .

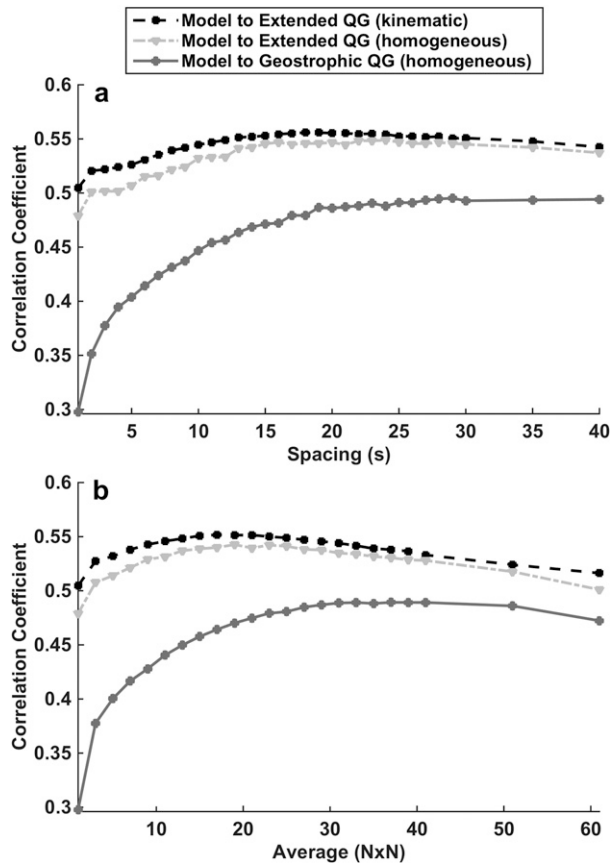


FIG. 7. Entire column model and QG  $\omega$  correlation values for 1800 UTC 12 Dec 2010 for the (a) cross method and (b) box method. Type of initial condition in parentheses.

result of the ageostrophic motions included in the extended cases. As the flow pattern is highly amplified, the winds in the trough and ridge axes follow gradient balance, causing larger ageostrophic motions.

#### b. Four additional cases

We now take a more cursory analysis of four additional cases with the geostrophically forced QG  $\omega$  using homogeneous initial conditions and extended QG  $\omega$  using kinematic initial conditions. The four cases are 1200 UTC 30 January 2013, 1200 UTC 2 February 2015, 1200 UTC 30 March 2014, and 1200 UTC 9 April 2014. As before,  $s$  was allowed to vary between 1 and 40, and  $N$  varied between 1 and 61. The entire column correlation between QG and NAM  $\omega$  is shown in Fig. 9 for the cross method (Figs. 9a,c) and the box method (Figs. 9b,d), with the results from case one included for comparison. The shape of the curves is similar between each case and both methods. Correlations rapidly increase up to  $s = 10$  or  $N = 15$ , experience a slow period of increase, then either level off or slowly decrease beyond  $s = 20$  or  $N = 25$ . The lowest correlations at the smallest  $s$  or  $N$  vary

between 0.1 and 0.32 for the geostrophic QG  $\omega$  and between 0.24 and 0.5 for the extended QG  $\omega$ . There is a range of highest correlations from 0.35 to 0.55 for the extended  $\omega$  and from 0.25 to 0.5 for the geostrophic  $\omega$ , but those highest correlations occur near the same values of  $s$  and  $N$  ( $s \approx 20$  and  $N \approx 21$ ).

The vertical motion from the NAM and the  $s = 20$  and  $N = 21$  spacings is shown for the January and February cases in Fig. 10 and for the March and April cases in Fig. 11. Each of the four cases contains a trough in various stages of development over or near the eastern United States. The January case (Figs. 10a–e) consists of a trough over the Mississippi River valley with a large area of vertical motion downstream. The  $s = 20$  and  $N = 21$  trials show moderate agreement with NAM values (correlations shown in headings of each panel in Fig. 10), with the strongest ascent placed in southern Illinois, central Georgia, and New England. QG  $\omega$  does experience some difficulty with linear ascent features. The box method (Figs. 10c,e) has minima of stronger magnitude than the cross method (Figs. 10b,d), just as in the December case study. The February case (Figs. 10f–j) has more zonal flow, with a shortwave moving across the mid-Atlantic states. The NAM vertical motion field shows a large area of ascent off the east coast with strong descent over Mississippi. QG  $\omega$  matches these two broad features well with higher correlations than the January case; again, the box method (Figs. 10h,j) has higher magnitude ascent and descent than the cross method (Figs. 10g,i).

The March case study (Figs. 11a–e) consists of a closed low off the East Coast, with strong ascent over the open Atlantic, strong descent across the United States, and descent over the Great Lakes. Both the cross (Figs. 11b,d) and box (Figs. 11c,e) methods place the strongest areas of descent well over New York and Florida, but have less success placing the strongest ascent. Correlations for this case have similar values to the February case. Finally, the April case study (Figs. 11f–j) comprises a trough on the East Coast. There is strong ascent over the ocean and moderate descent over the continent. QG  $\omega$  agrees with NAM  $\omega$ , with strong descent over Cuba and ascent ahead of the trough. The correlations between extended QG  $\omega$  and NAM  $\omega$  for the April study are lower and in a similar range to the January case study. The highest correlated cases for the cross and box method for each of the four cases are similar, though there are slight differences in the magnitude and shape of the vertical motion maxima and minima.

The geostrophic versions of the forcing for each case (Figs. 10d,e,i,j and 11d,e,i,j) have QG  $\omega$  that is weaker in magnitude but with strong agreement in the placement of minima and maxima. There are local minima or maxima that are absent with the geostrophic QG  $\omega$ , but

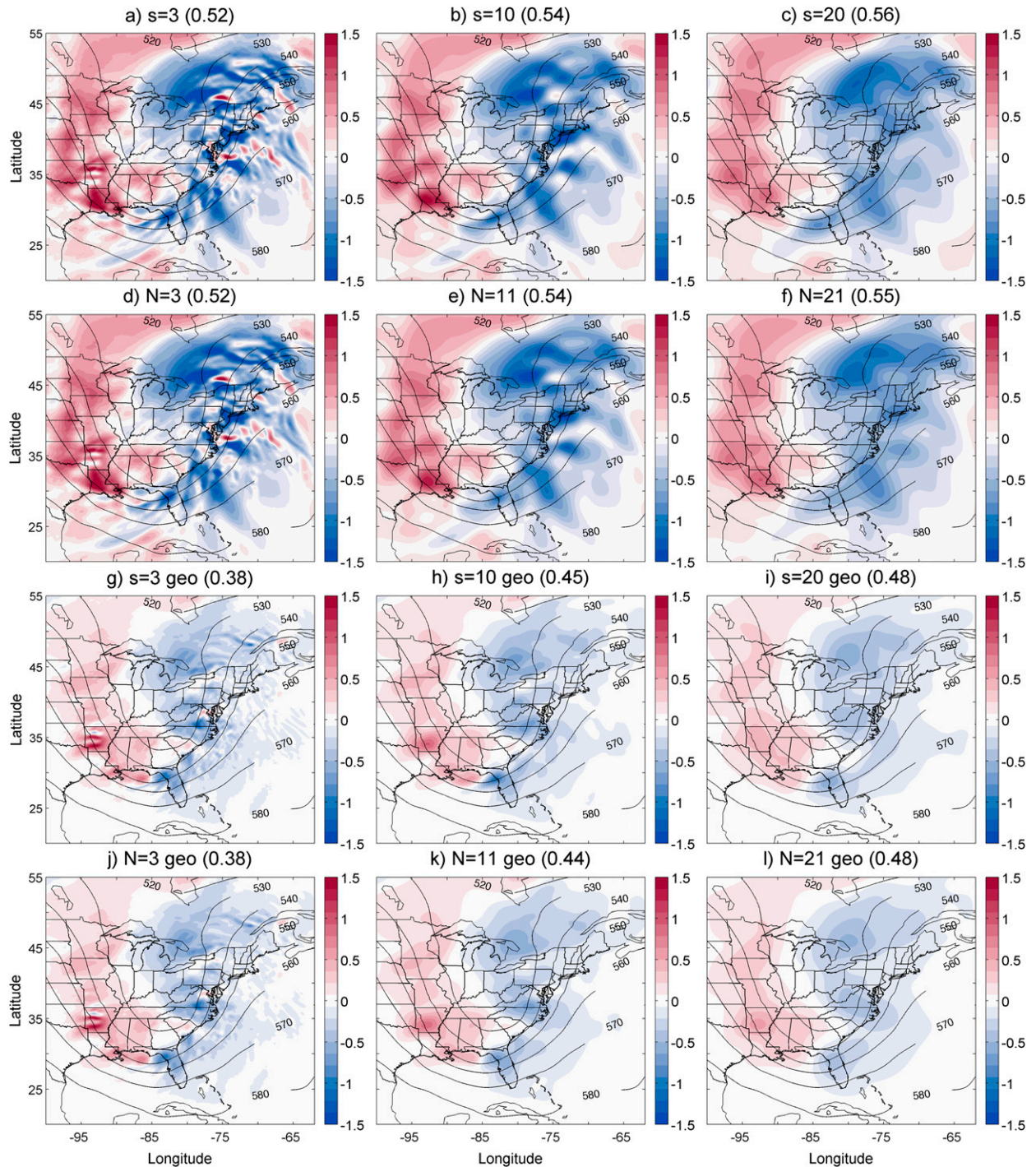


FIG. 8. As in Fig. 2, but with QG  $\omega$  ( $\text{Pa s}^{-1}$ ). Values in parentheses are full domain correlations to model  $\omega$ .

the qualitative situation is similar between the two forms of QG  $\omega$ . However, the correlations are between 20% and 30% smaller with the geostrophic QG  $\omega$  compared to the extended, due to the addition of ageostrophic advection from the NAM in the extended  $\omega$ . Nonetheless, these four additional cases show that at the correct

horizontal scale, both versions of QG  $\omega$  have great utility in diagnosing vertical motion on high-resolution data.

### c. Correlation analysis

From the five case studies, the smallest horizontal scale is empirically found to correspond to  $s = 12$  and  $N = 13$

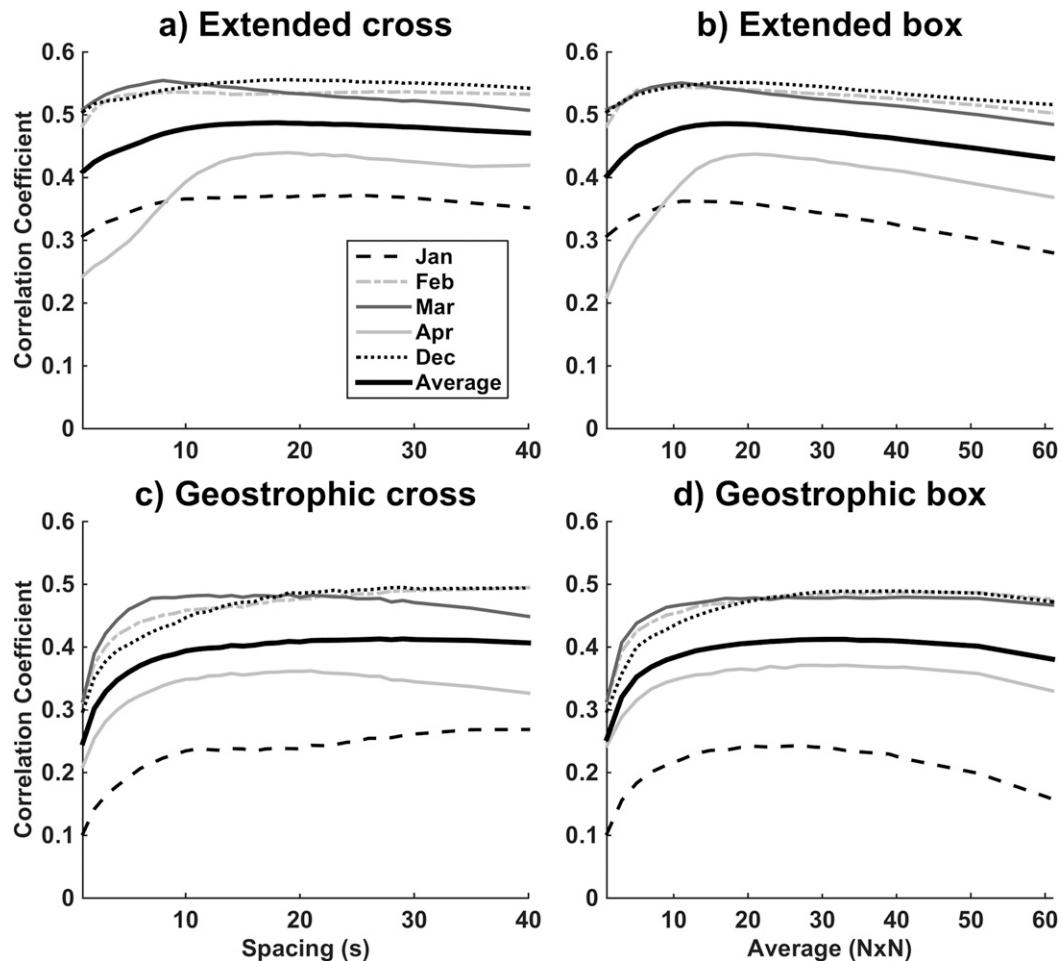


FIG. 9. Entire column model to QG  $\omega$  correlation values for the (a) extended cross method, (b) extended box method, (c) geostrophic cross method, and (d) geostrophic box method for 1200 UTC 30 Jan 2013, 1200 UTC 2 Feb 2015, 1200 UTC 30 Mar 2014, 1200 UTC 9 Apr 2014, and 1800 UTC 12 Dec 2010. Black line is the time average of the five cases used to find minimum spacing. (See text for more details.)

for the geostrophically forced QG  $\omega$  and  $s = 11$  and  $N = 15$  for the extended QG  $\omega$ . This determination is based on the inflection point of the average curve of the QG  $\omega$  to NAM  $\omega$  correlation. Geostrophic and extended QG  $\omega$  curves (Fig. 9) are separately averaged for both the box method and the cross method. A fifth-order polynomial is fit to the curves, and the roots of the second derivative are found. The smallest root for each polynomial corresponds to the inflection point of the curve and is the location where the correlations cease increasing rapidly and level off. Any further increase in the horizontal spacing beyond this inflection point gains only slightly in correlation back to NAM  $\omega$  to the detriment of resolution.

In total, 23 more cases were evaluated using geostrophic and extended QG  $\omega$  at the native resolution ( $s = 1$ ), the smallest  $N$  value ( $N = s = 3$ ), and a value of  $s$  and  $N$  above the size of the highest correlated trials ( $s = 20$  and  $N = 21$ ). The resulting full-column correlations back to the NAM

values are given in Table 2. The lowest full-column correlation at  $s = 1$  for the geostrophic QG  $\omega$  is 0.1 and for the extended QG  $\omega$  is 0.24. The highest correlation for extended QG  $\omega$  for both methods is 0.57 and for geostrophic QG  $\omega$  is 0.54. There appears to be no seasonal or yearly trend to the performance of either method. The average correlation for the geostrophic QG  $\omega$  at native resolution is  $0.25 \pm 0.06$  and  $0.42 \pm 0.07$  for extended QG  $\omega$ . At  $s = 20$  and  $N = 21$ , geostrophic QG  $\omega$  has an average correlation of  $0.42 \pm 0.06$  and extended QG  $\omega$  has an average correlation of  $0.48 \pm 0.05$ .

## 6. Discussion

Research using the QG  $\omega$  equation continues to be widespread, but the datasets on which QG  $\omega$  is assessed are increasing in resolution. While the theoretical length scale at which QG motions are usable is well known, there

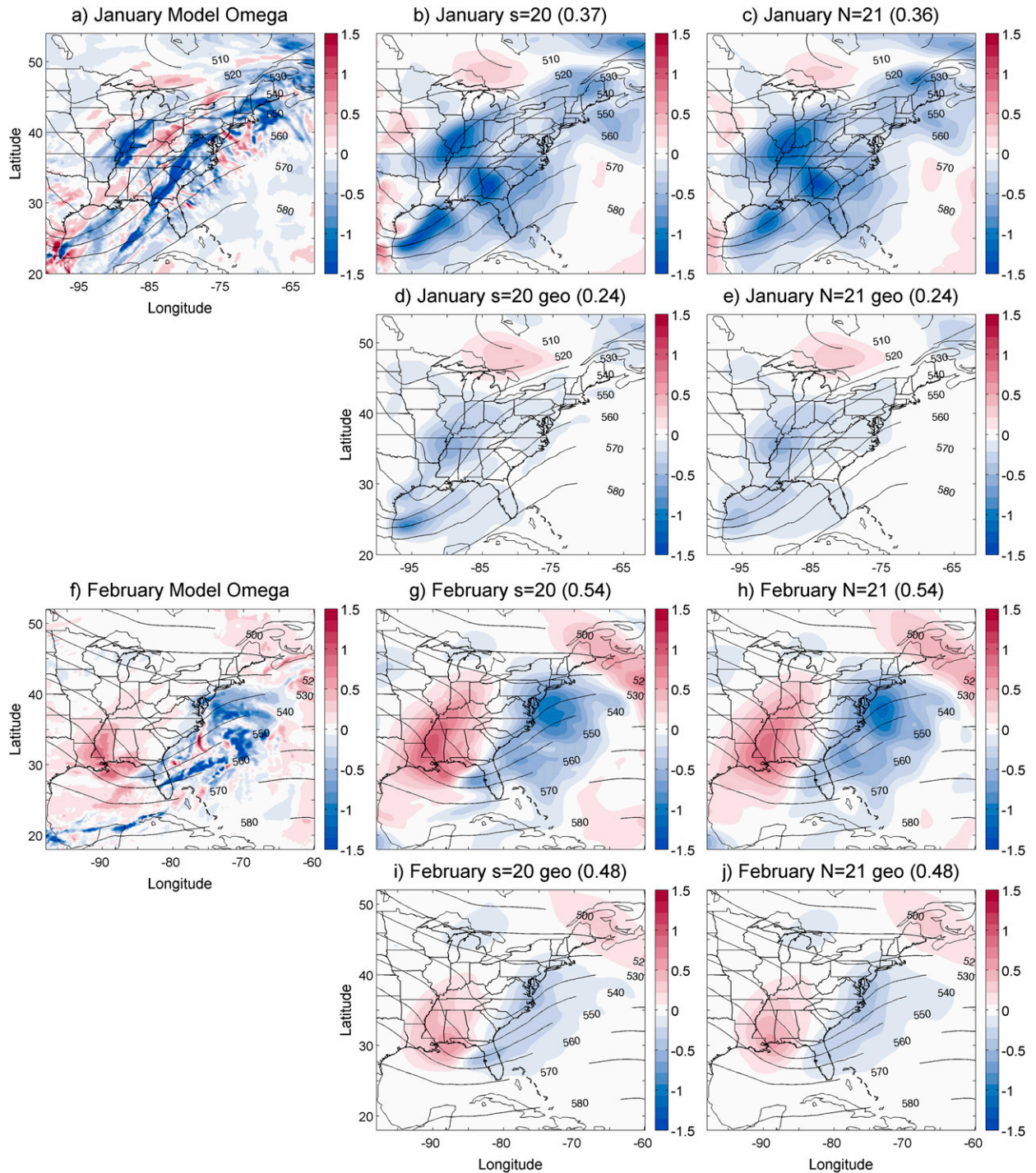


FIG. 10. The  $\omega$  ( $\text{Pa s}^{-1}$ ) at 500 hPa at (a)–(e) 1200 UTC 30 Jan 2013 and at (f)–(j) 1200 UTC 2 Feb 2015 from the (a),(f) NAM, extended QG  $\omega$  using the (b),(g) cross method and (c),(h) box method, and geostrophic QG  $\omega$  using the (d),(i) cross method and (e),(j) box method. Values in parentheses are full domain correlation to model  $\omega$ .

has been no empirical study to evaluate the optimum length scale on model or reanalysis data. The traditional form of the QG  $\omega$  equation in an extended form and with the usual geostrophic forcing has been evaluated to

determine at what horizontal scale assessments of vertical motion provide the optimal estimation compared to model diagnosed fields. To test the horizontal distances, two methods were used to upscale the state variables from

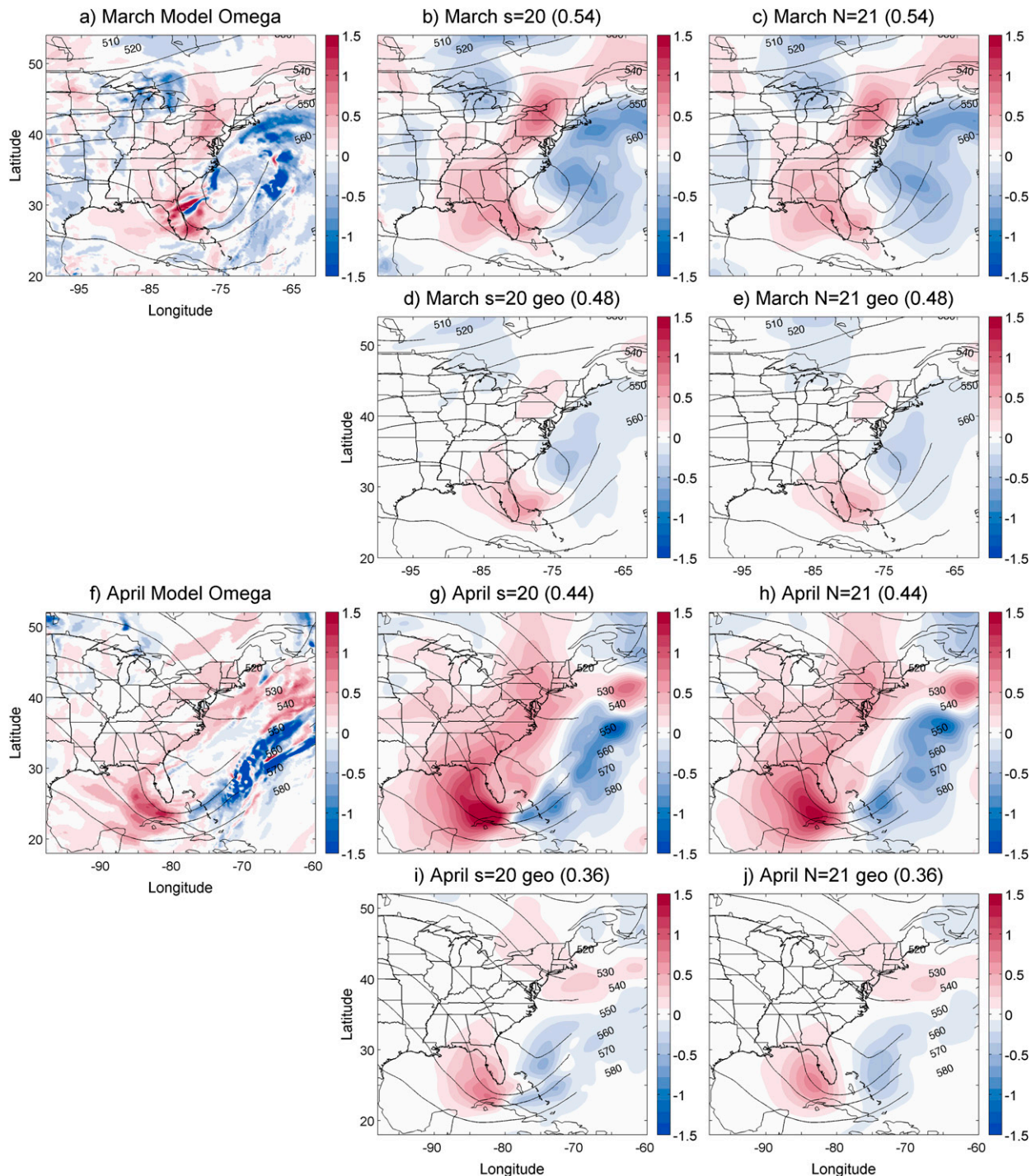


FIG. 11. As in Fig. 10, but at (a)–(e) 1200 UTC 30 Mar 2014 and (f)–(j) 1200 UTC 9 Apr 2014.

the operational NAM. The cross method stretches the finite-differencing scheme by sampling the fields at increasing distances, ensuring any features below the scaling threshold are neglected. The box method assigns an average of surrounding values in a box to a central

point—smoothing out subsynoptic-scale waves—then performing the finite differencing at native resolution. The forcing functions, and thus the final  $\omega$  field, become more synoptic in scale as spacing or box size is increased. QG  $\omega$  was evaluated on 28 synoptic systems and

TABLE 2. Correlation between QG geostrophic (geo) and extended  $\omega$  and NAM  $\omega$  between 975 and 75 hPa for 28 cases at three spacings. Error bounds are standard deviation.

Date	$s = 1$	$s = 3$	$s = 20$	$N = 3$	$N = 21$	$s = 1$ geo	$s = 3$ geo	$s = 20$ geo	$N = 3$ geo	$N = 21$ geo
1200 UTC 3 Jan 2012	0.54	0.57	0.54	0.58	0.54	0.28	0.34	0.43	0.34	0.44
0000 UTC 12 Jan 2014	0.35	0.38	0.43	0.38	0.42	0.23	0.30	0.38	0.30	0.36
1200 UTC 17 Jan 2016	0.42	0.47	0.53	0.48	0.53	0.20	0.27	0.45	0.29	0.44
1200 UTC 24 Jan 2015	0.37	0.42	0.48	0.43	0.47	0.14	0.22	0.33	0.23	0.35
1200 UTC 30 Jan 2013	0.31	0.33	0.37	0.33	0.36	0.10	0.10	0.23	0.16	0.24
1200 UTC 2 Feb 2015	0.48	0.52	0.53	0.53	0.54	0.31	0.40	0.48	0.40	0.48
1200 UTC 5 Feb 2016	0.48	0.53	0.57	0.54	0.57	0.21	0.30	0.51	0.31	0.52
0000 UTC 25 Feb 2012	0.45	0.48	0.52	0.49	0.52	0.23	0.30	0.44	0.31	0.44
0000 UTC 25 Feb 2016	0.42	0.47	0.49	0.30	0.49	0.20	0.29	0.44	0.48	0.44
1200 UTC 4 Mar 2012	0.41	0.43	0.53	0.44	0.52	0.25	0.32	0.41	0.33	0.43
0000 UTC 28 Mar 2015	0.37	0.40	0.43	0.41	0.42	0.18	0.25	0.36	0.25	0.35
1200 UTC 30 Mar 2014	0.53	0.57	0.53	0.57	0.54	0.31	0.42	0.48	0.42	0.48
0000 UTC 31 Mar 2014	0.47	0.51	0.49	0.51	0.49	0.28	0.36	0.43	0.36	0.43
0000 UTC 8 Apr 2014	0.24	0.44	0.50	0.45	0.50	0.21	0.37	0.44	0.37	0.43
1200 UTC 9 Apr 2014	0.41	0.27	0.44	0.27	0.44	0.30	0.28	0.36	0.29	0.36
1200 UTC 12 Apr 2011	0.40	0.41	0.42	0.42	0.43	0.27	0.34	0.40	0.34	0.40
1200 UTC 21 Apr 2012	0.33	0.38	0.44	0.39	0.44	0.21	0.29	0.40	0.30	0.40
0000 UTC 2 Oct 2011	0.37	0.40	0.38	0.40	0.38	0.21	0.27	0.32	0.27	0.33
1200 UTC 29 Oct 2012	0.54	0.56	0.50	0.56	0.49	0.27	0.36	0.43	0.34	0.42
1200 UTC 29 Oct 2015	0.39	0.42	0.39	0.42	0.39	0.18	0.26	0.32	0.25	0.31
1200 UTC 4 Nov 2011	0.52	0.56	0.56	0.57	0.55	0.43	0.49	0.54	0.50	0.54
0000 UTC 13 Nov 2013	0.48	0.51	0.49	0.52	0.48	0.34	0.40	0.42	0.40	0.42
1200 UTC 12 Nov 2015	0.40	0.47	0.53	0.49	0.53	0.30	0.39	0.50	0.40	0.50
0000 UTC 21 Nov 2012	0.38	0.43	0.46	0.43	0.46	0.27	0.39	0.44	0.40	0.45
0000 UTC 13 Dec 2010	0.50	0.52	0.56	0.53	0.55	0.30	0.38	0.49	0.38	0.47
0000 UTC 11 Dec 2015	0.41	0.45	0.43	0.45	0.43	0.28	0.37	0.40	0.38	0.42
1200 UTC 21 Dec 2012	0.46	0.49	0.54	0.50	0.54	0.33	0.39	0.50	0.39	0.49
1200 UTC 25 Dec 2014	0.36	0.40	0.44	0.41	0.45	0.28	0.35	0.40	0.35	0.40
Avg	0.42 ± 0.07	0.45 ± 0.07	0.48 ± 0.05	0.45 ± 0.08	0.48 ± 0.05	0.25 ± 0.06	0.33 ± 0.07	0.42 ± 0.06	0.33 ± 0.07	0.42 ± 0.06

correlated back to NAM vertical motion for an extensive array of cross and box sizes. Taken as a whole, both methods perform as expected, with resulting QG  $\omega$  values nearly indistinguishable between the two methods.

Correlations between QG and NAM  $\omega$  are highest in the midlevels and decrease above 200 hPa and below 800 hPa for each method for both the extended and geostrophic forms (Fig. 6). Above 200 hPa, correlations decrease quickly because vertical motion in the NAM is not constrained to  $0 \text{ Pa s}^{-1}$  at the top level of 50 hPa, while both versions of QG  $\omega$  are constrained at this level. The effect of that constant boundary is carried through the subsequent lower layers. More importantly, the tropopause occurs near 200 hPa, and vertical motion patterns and magnitude change substantially in the stratosphere. Additionally, errors in vertical discretization will grow much larger near the top of the model domain since the height spacing between the constant 25-hPa levels grows exponentially. Below 800 hPa, correlations decrease due to ignorance of the boundary layer height and thus interaction with surface friction. Evident from Fig. 6 is the improvement in the correlations for QG  $\omega$  in the midlevels with larger  $s$  or  $N$ . Correlations between geostrophic QG  $\omega$  and the model value peak at approximately 0.5 for  $s = N = 3$  between 700 and 200 hPa but are near 0.6 at  $s = 10$  and  $N = 11$ . However, much of the improvement for the column total correlation at large spacing comes at the top and bottom of the atmosphere. The shape of the vertical correlation function is similar to that of Räisänen (1995), who found an average vertical correlation between a QG  $\omega$  and a general  $\omega$  to be near 0.7 for the midlatitudes, with maximum correlations at the midlevels and minima near the surface and upper levels.

The correlation between QG  $\omega$  and NAM  $\omega$  increases as  $s$  or  $N$  increases. The geostrophic QG  $\omega$  correlation peaks around 0.45 for  $s = N = 10$  for the December, February, and March cases but starts at 0.3 for  $s = 1$ . The January and April correlations are initially lower, below 0.2 at  $s = 1$  but climb quickly (Fig. 9). At large values of  $s$  or  $N$ , the geostrophic correlations are approximately 50% larger than at small distances. Correlations for each case converge to that of the extended QG  $\omega$  as the horizontal spacing increases because the ageostrophic component of the wind becomes smaller.

The relationship between correlation to NAM  $\omega$  and increasing horizontal spacing is weaker for the extended QG  $\omega$  despite the correlations being slightly higher than those of geostrophic QG  $\omega$ . We attribute the smaller improvement in the extended QG  $\omega$  to the full horizontal wind from the model refining the advection in the forcing functions at the smaller distances. For the cross method on the extended QG  $\omega$ , correlations climb above  $s = 1$ , then level off after  $s = 10$  near 0.55 for the December,

February, and March cases and 0.35 for the January and April cases (Fig. 9a). The box method correlation values climb from  $N = 1$  to  $N = 10$ , with a value of 0.55 for December, February, and March and around 0.35 for January and April, then slowly decrease for larger  $N$  values (Fig. 9b). Even in cases where the final QG solution is not highly correlated to the model solution (i.e., January or April cases), lengthening the horizontal scale over which the calculations are performed increases the correlation between QG and NAM  $\omega$ . Furthermore, at small spacings, the final  $\omega$  fields for the December case study have localized areas of large magnitude descent in the middle of the cyclone (Figs. 8a,d) that are not present in the NAM model fields (Fig. 1d). For this reason, we find that any evaluation of QG  $\omega$  should be done by upscaling the state variables before calculation of the QG forcing functions as opposed to spectrally removing higher wavenumber components from  $\omega$  evaluated at full resolution.

In addition to the results from a horizontally averaged one-dimensional (1D)  $\sigma$ , a fully three-dimensional (3D)  $\sigma$  was attempted, following Vasilj and Smith (1997). While at large horizontal scales the results were similar to the 1D  $\sigma$ , the results at smaller distances were unrealistic, with strong descent in the middle of the cyclone in the January, February, and December cases. The failure of QG  $\omega$  at small length scales with the 3D  $\sigma$  is a practical demonstration of the theoretical flaw in allowing the static stability to vary horizontally in the QG  $\omega$  equation. The derivation of the QG  $\omega$  equation requires  $\sigma$  to be constant horizontally or the inclusion of terms in the lhs of the QG  $\omega$  equation to account for the horizontal variation; namely,  $1/\sigma(\omega\nabla_h^2\sigma + 2\nabla_h\sigma \cdot \nabla_h\omega)$ . To maintain the elliptical nature of the QG  $\omega$  equation,  $\sigma$  must remain positive. Forcing  $\sigma$  to a positive value creates discontinuities in these terms.

The two upscaling techniques yield nearly identical results for correlations back to NAM  $\omega$ . Using five case studies, the horizontal scale where correlations cease increasing rapidly was found, and 23 more cases were calculated above those respective  $s$  and  $N$  values. For  $s = 20$  and  $N = 21$ , the geostrophic QG  $\omega$  is correlated to NAM  $\omega$  at  $0.42 \pm 0.06$ , and the extended  $\omega$  at  $0.48 \pm 0.05$  (Table 2). The cross method does not reduce the power of higher wavenumber forcing features as strongly as the box method at smaller length scales, but  $\omega$  itself is reduced at high wavenumbers equally for both methods (Fig. 5). Vertical correlations (Fig. 6) between the two methods are comparable at equal length scales. Qualitatively, the QG forcing functions are smoother for a given  $N$  value than the same  $s$  value (Fig. 4). This could make interpretation of the forcing functions easier with the box method.

Comparing the two scaling methods, smaller values of  $s$  and  $N$  are more correlated to each other (Table 1). At

small  $N$ , there are few points averaged into the box method that are also not included in the cross method. As  $N$  increases, the number of points used by the box method increases  $\propto N^2$ , so the solutions diverge. The reason for testing the cross method was practical, in that the cross method can reach a smaller horizontal distance at  $s = 2$ , while the box method cannot average any smaller than three points on an edge. However, this leads to a deficiency in the cross method. The cross method must operate on a difference calculation, while the box method can work on any field independently of the operator. This is an issue if three-dimensional static stability is used. Therefore, it is concluded that the box method is marginally better than the cross method, unless the required resolution is below that achievable by the box method.

Finally, the smallest horizontal length scale to evaluate QG  $\omega$  and its forcing is found to be  $L \approx 140$  km. This value is empirically found from both the box and cross methods for both the extended and geostrophic QG  $\omega$  based on the correlation back to NAM vertical motion. The length scale is based on the inflection point of a polynomial fit to the average correlations for a large range of  $s$  and  $N$  values for five cases. While some correlations of the 28 cases studied, including the January case that is part of the estimate of the length scale, are quite low, the behavior of increasing correlation with increasing  $s$  or  $N$  is robust across all cases so that above the lowest length scale, QG  $\omega$  is as high as practical. We attribute the differences in some correlations between cases to two possibilities: 1) interseasonal and interannual variability, and, more importantly, 2) analyzing different stages of cyclone development with different cases. In the case of possibility two, we deliberately chose instances across the development cycle to find a general estimate of length scale as opposed to a series of scales for different stages of cyclone evolution. The value of  $L$  found here is smaller than that found by Barnes et al. (1996) that determined a 15-point filter on a 29-km resolution model was best with a 19-point filter being too smooth. The equivalent resolution on a 12-km grid is a 35-point filter, which is considerably larger than the  $N = 13$  value found here. This is a consequence of Barnes et al. (1996) investigating the forcing functions of QG  $\omega$  and not  $\omega$  itself. Because of the second derivatives on the lhs of the QG  $\omega$  equation, small-scale features are less pronounced in  $\omega$  than in the forcing, which tends to reduce the need for filtering (cf. right columns of Figs. 4 and 8).

## 7. Conclusions

Quasigeostrophic  $\omega$  is frequently used to diagnose the causes of vertical motion for a wide range of applications; however, the limits of the applicability of QG  $\omega$  are being

approached as reanalysis and model output increase in resolution. For QG theory to continue to be valid, high-resolution data must be upscaled. This optimization is necessary because some studies use QG  $\omega$  on high-resolution models without accounting for the reduced horizontal distances between grid points. QG analysis can still be achieved with a high-resolution model to great effect in the midlevels (750–200 hPa) by lengthening the horizontal scale of derivative calculations to the synoptic scale. Above a length scale of  $L \approx 140$  km, an “extended” QG  $\omega$  is found to be correlated at  $0.48 \pm 0.05$  for 28 cases to NAM  $\omega$ . This result indicates that future studies of synoptic-scale phenomena that use QG  $\omega$  should average or sample values of state variables and each horizontal calculation. In this way, QG analysis can be performed on high-resolution datasets to understand vertical motion in the midlatitudes.

Future work will include methods to assess the vertical skill of the scaling methods by incorporating information on the boundary layer and tropopause along with the diabatic forcing term. Additional QG variables, such as geopotential tendency and vorticity, will also be investigated to determine if their skill is improved in a similar way as QG  $\omega$ . Other work will include empirically ascertaining the relationship between the stage of cyclone development or cyclone type (Petterssen and Smebye 1971) and suitability of QG  $\omega$  along with other forms of the omega equation, like the Sutcliffe–Trenberth (Sutcliffe 1947; Trenberth 1978) form.

*Acknowledgments.* MB was supported partially by the American Meteorological Society through a 21st Century Campaign Graduate Fellowship. Dr. P. Grady Dixon reviewed an earlier draft of the manuscript. Dr. Phil Amburn and Mr. Jacob Bowen provided code for accessing and indexing VTK arrays. Mr. Michael Herrera assisted with analysis of the power spectrum. The manuscript was greatly improved by the detailed comments of several anonymous reviewers.

## REFERENCES

- Barnes, S. L., and B. R. Colman, 1993: Quasigeostrophic diagnosis of cyclogenesis associated with a cutoff extratropical cyclone—The Christmas 1987 Storm. *Mon. Wea. Rev.*, **121**, 1613–1634, doi:10.1175/1520-0493(1993)121<1613:QDOCAW>2.0.CO;2.
- , F. Caracena, and A. Marroquin, 1996: Extracting synoptic-scale diagnostic information from the mesoscale models: The Eta model, gravity waves, and quasigeostrophic diagnostics. *Bull. Amer. Meteor. Soc.*, **77**, 519–528, doi:10.1175/1520-0477(1996)077<0519:ESSDIF>2.0.CO;2.
- Billingsley, D., 1997: Review of QG theory—Part II: The omega equation. *Natl. Wea. Dig.*, **21** (2), 43–51.
- Davies, H. C., 2015: The quasigeostrophic omega equation: Reappraisal, refinements, and relevance. *Mon. Wea. Rev.*, **143**, 3–25, doi:10.1175/MWR-D-14-00098.1.

- Durran, D. R., and L. W. Snellman, 1987: The diagnosis of synoptic-scale vertical motion in an operational environment. *Wea. Forecasting*, **2**, 17–31, doi:10.1175/1520-0434(1987)002<0017:TDOSSV>2.0.CO;2.
- Finch, Z. O., and R. H. Johnson, 2010: Observational analysis of an upper-level inverted trough during the 2004 North American Monsoon Experiment. *Mon. Wea. Rev.*, **138**, 3540–3555, doi:10.1175/2010MWR3369.1.
- Fjørtoft, R., 1955: On the use of space-smoothing in physical weather forecasting. *Tellus*, **7A**, 462–480, doi:10.1111/j.2153-3490.1955.tb01185.x.
- Gao, S., Z. Meng, F. Zhang, and L. F. Bosart, 2009: Observational analysis of heavy rainfall mechanisms associated with severe Tropical Storm Bilis (2006) after its landfall. *Mon. Wea. Rev.*, **137**, 1881–1897, doi:10.1175/2008MWR2669.1.
- Gyakum, J. R., 1991: Meteorological precursors to the explosive intensification of the QE II storm. *Mon. Wea. Rev.*, **119**, 1105–1131, doi:10.1175/1520-0493(1991)119<1105:MPTTEI>2.0.CO;2.
- Hart, N. C. G., C. J. C. Reason, and N. Fauchereau, 2010: Tropical–extratropical interactions over southern Africa: Three cases of heavy summer season rainfall. *Mon. Wea. Rev.*, **138**, 2608–2623, doi:10.1175/2010MWR3070.1.
- Holton, J. R., 2004: *An Introduction to Dynamic Meteorology*. 4th ed. Academic Press, 535 pp.
- Hoskins, B. J., I. Draghici, and H. C. Davies, 1978: A new look at the  $\omega$ -equation. *Quart. J. Roy. Meteor. Soc.*, **104**, 31–38, doi:10.1256/smsqj.43902.
- Hryciw, L. M., E. H. Atallah, S. M. Milrad, and J. R. Gyakum, 2013: A meteorological analysis of important contributors to the 1999–2005 Canadian Prairie drought. *Mon. Wea. Rev.*, **141**, 3593–3609, doi:10.1175/MWR-D-12-00261.1.
- Jusem, J. C., and R. Atlas, 1998: Diagnostic evaluation of vertical motion forcing mechanisms by using Q-vector partitioning. *Mon. Wea. Rev.*, **126**, 2166–2184, doi:10.1175/1520-0493(1998)126<2166:DEOVMF>2.0.CO;2.
- Kolmogorov, A. N., 1941: The local structure of turbulence in incompressible viscous fluid for very large Reynolds numbers. *Proc. Acad. Sci. USSR, Geochem. Sect.*, **30**, 299–303.
- Krishnamurti, T. N., 1968: A diagnostic balance model for studies of weather systems of low and high latitudes, Rossby number less than 1. *Mon. Wea. Rev.*, **96**, 197–207, doi:10.1175/1520-0493(1968)096<0197:ADBMFS>2.0.CO;2.
- Lang, A. A., and J. E. Martin, 2010: The influence of rotational frontogenesis and its associated shearwise vertical motions on the development of an upper-level front. *Quart. J. Roy. Meteor. Soc.*, **136**, 239–252, doi:10.1002/qj.551.
- Lareau, N. P., and J. D. Horel, 2012: The climatology of synoptic-scale ascent over western North America: A perspective on storm tracks. *Mon. Wea. Rev.*, **140**, 1761–1778, doi:10.1175/MWR-D-11-00203.1.
- Lovejoy, S., and D. Schertzer, 2010: Towards a new synthesis for atmospheric dynamics: Space-time cascades. *Atmos. Res.*, **96**, 1–52, doi:10.1016/j.atmosres.2010.01.004.
- Lupo, A. R., P. J. Smith, and P. Zwack, 1992: A diagnosis of the explosive development of two extratropical cyclones. *Mon. Wea. Rev.*, **120**, 1490–1523, doi:10.1175/1520-0493(1992)120<1490:ADOTED>2.0.CO;2.
- Martin, J. E., 2014: Quasi-geostrophic diagnosis of the influence of vorticity advection on the development of upper level jet-front systems. *Quart. J. Roy. Meteor. Soc.*, **140**, 2658–2671, doi:10.1002/qj.2333.
- Milrad, S. M., E. H. Atallah, and J. R. Gyakum, 2010: Synoptic typing of extreme cool-season precipitation events at St. Johns, Newfoundland, 1979–2005. *Wea. Forecasting*, **25**, 562–586, doi:10.1175/2009WAF2222301.1.
- Mudrick, S. E., 1974: A numerical study of frontogenesis. *J. Atmos. Sci.*, **31**, 869–892, doi:10.1175/1520-0469(1974)031<0869:ANSOF>2.0.CO;2.
- O'Brien, J., 1970: Alternative solutions to the classical vertical velocity problem. *J. Appl. Meteor.*, **9**, 197–203, doi:10.1175/1520-0450(1970)009<0197:ASTTCV>2.0.CO;2.
- Pauley, P. M., and S. J. Nieman, 1992: A comparison of quasigeostrophic and nonquasigeostrophic vertical motions for a model-simulated rapidly intensifying marine extratropical cyclone. *Mon. Wea. Rev.*, **120**, 1108–1134, doi:10.1175/1520-0493(1992)120<1108:ACQAN>2.0.CO;2.
- Pettersen, S., and S. J. Smebye, 1971: On the development of extratropical cyclones. *Quart. J. Roy. Meteor. Soc.*, **97**, 457–482, doi:10.1002/qj.49709741407.
- Räsänen, J., 1995: Factors affecting synoptic-scale vertical motions: A statistical study using a generalized omega equation. *Mon. Wea. Rev.*, **123**, 2447–2460, doi:10.1175/1520-0493(1995)123<2447:FASSVM>2.0.CO;2.
- Ressler, G. M., S. M. Milrad, E. H. Atallah, and J. R. Gyakum, 2012: Synoptic-scale analysis of freezing rain events in Montreal, Quebec, Canada. *Wea. Forecasting*, **27**, 362–378, doi:10.1175/WAF-D-11-00071.1.
- Sinclair, M. R., 1993: A diagnostic study of extratropical precipitation resulting from Tropical Cyclone Bola. *Mon. Wea. Rev.*, **121**, 2690–2707, doi:10.1175/1520-0493(1993)121<2690:ADSOTE>2.0.CO;2.
- Smith, P. J., and C. P. Lin, 1978: A comparison of synoptic-scale vertical motions computed by the kinematic method and two forms of the omega equation. *Mon. Wea. Rev.*, **106**, 1687–1694, doi:10.1175/1520-0493(1978)106<1687:ACOSSV>2.0.CO;2.
- Stuart, D. W., and T. H. R. O. Neill, 1967: The over-relaxation factor in the numerical solution of the omega equation. *Mon. Wea. Rev.*, **95**, 303–307, doi:10.1175/1520-0493(1967)095<0303:TORFIT>2.3.CO;2.
- Surcel, M., I. Zawadzki, and M. K. Yau, 2016: The case-to-case variability of the predictability of precipitation by a Storm-Scale Ensemble Forecasting system. *Mon. Wea. Rev.*, **144**, 193–212, doi:10.1175/MWR-D-15-0232.1.
- Sutcliffe, R. C., 1947: A contribution to the problem of development. *Quart. J. Roy. Meteor. Soc.*, **73**, 370–383, doi:10.1002/qj.49707331710.
- Trenberth, K. E., 1978: On the interpretation of the diagnostic quasi-geostrophic omega equation. *Mon. Wea. Rev.*, **106**, 131–137, doi:10.1175/1520-0493(1978)106<0131:OTIOTD>2.0.CO;2.
- Tsou, C., and P. J. Smith, 1990: The role of synoptic/planetary-scale interactions during the development of a blocking anticyclone. *Tellus*, **42A**, 174–193, doi:10.1034/j.1600-0870.1990.00015.x.
- , —, and P. M. Pauley, 1987: A comparison of adiabatic and diabatic forcing in an intense extratropical cyclone system. *Mon. Wea. Rev.*, **115**, 763–786, doi:10.1175/1520-0493(1987)115<0763:ACQAD>2.0.CO;2.
- Vasilj, J. M., and P. J. Smith, 1997: A comparison of extended and quasigeostrophic dynamics for a case of small Rossby number extratropical cyclone development. *Mon. Wea. Rev.*, **125**, 3347–3356, doi:10.1175/1520-0493(1997)125<3347:ACQEAQ>2.0.CO;2.
- Wiin-Nielsen, A., 1959: On a graphical method for an approximate determination of the vertical velocity in the mid-troposphere. *Tellus*, **11A**, 432–440, doi:10.1111/j.2153-3490.1959.tb00053.x.
- Zwack, P., and B. Okosssi, 1986: A new method for solving the quasi-geostrophic omega equation by incorporating surface pressure tendency data. *Mon. Wea. Rev.*, **114**, 655–666, doi:10.1175/1520-0493(1986)114<0655:ANMFST>2.0.CO;2.